Computers in Biology and Medicine 136 (2021) 104768

Contents lists available at ScienceDirect

Computers in Biology and Medicine

journal homepage: www.elsevier.com/locate/compbiomed

Unraveling the permeation of reactive species across nitrated membranes by computer simulations

Maria C. Oliveira [a,b], Maksudbek Yusupov [a,c], Rodrigo M. Cordeiro [b], Annemie Bogaerts [a,*]

[a] Research Group PLASMANT, Department of Chemistry, University of Antwerp, Universiteitsplein 1, B-2610, Antwerp, Belgium
[b] Centro de Ciências Naturais e Humanas, Universidade Federal do ABC, Avenida dos Estados 5001, CEP 09210-580, Santo André, SP, Brazil
[c] Laboratory of Thermal Physics of Multiphase Systems, Arifov Institute of Ion-Plasma and Laser Technologies, Academy of Sciences of Uzbekistan, Durmon yuli str. 33, 100125, Tashkent, Uzbekistan

ARTICLE INFO

Keywords:
Reactive oxygen and nitrogen species
Nitro-oxidative stress
Molecular dynamics simulations
Nitrated membranes

ABSTRACT

Reactive oxygen and nitrogen species (RONS) are involved in many biochemical processes, including nitro-oxidative stress that causes cancer cell death, observed in cancer therapies such as photodynamic therapy and cold atmospheric plasma. However, their mechanisms of action and selectivity still remain elusive due to the complexity of biological cells. For example, it is not well known how RONS generated by cancer therapies permeate the cell membrane to cause nitro-oxidative damage. There are many studies dedicated to the permeation of RONS across native and oxidized membranes, but not across nitrated membranes, another lipid product also generated during nitro-oxidative stress. Herein, we performed *molecular dynamics* (MD) simulations to calculate the free energy barrier of RONS permeation across nitrated membranes. Our results show that hydrophilic RONS, such as hydroperoxyl radical (HO_2) and peroxynitrous acid (ONOOH), have relatively low barriers compared to hydrogen peroxide (H_2O_2) and hydroxyl radical (HO), and are more prone to permeate the membrane than for the native or peroxidized membranes, and similar to aldehyde-oxidized membranes. Hydrophobic RONS like molecular oxygen (O_2), nitrogen dioxide (NO_2) and nitric oxide (NO) even have insignificant barriers for permeation. Compared to native and peroxidized membranes, nitrated membranes are more permeable, suggesting that we must not only consider oxidized membranes during nitro-oxidative stress, but also nitrated membranes, and their role in cancer therapies.

1. Introduction

During the last decades, various cancer types have been developing resistance to traditional treatments, including radiation therapy [1], chemotherapy [2] and surgery. Likewise, many bacteria have become resistant to the antibiotics available in medicine. Non-thermal plasma, also called *cold atmospheric plasma* (CAP), has emerged as a therapeutic modality against bacteria [3,4] and against a wide variety of cancer types [5], including hepatocellular carcinoma [6], lung carcinoma [7], breast cancer [8], melanoma [9], glioblastoma [10], pancreatic cancer [11], and head and neck cancer [12].

Plasma, also referred as the fourth state of matter, is an ionized gas, consisting of electrons, ions and neutral species [13]. In CAP sources, plasma is created in gases such as air, O_2, N_2, He and Ar (flowing into ambient air), and it contains highly energetic and reactive species. These include *reactive oxygen and nitrogen species* (RONS), such as hydrogen peroxide (H_2O_2), hydroperoxyl radical (HO_2), hydroxyl radical (HO), singlet oxygen ($^1O_2$), nitrogen dioxide (NO_2), nitric oxide (NO), and peroxynitrous acid (ONOOH). It is now well established that the anti-microbial and anti-cancer capacity of CAP is based on the interaction of these RONS with microorganisms (bacteria, fungi, and viruses) [4,14] and with the surface of cancer cells [15,16]. In the anti-microbial capacity, the RONS trigger chain reactions to disrupt the metabolism of the microorganisms, resulting in cell membrane damage, leakage of intracellular macromolecules and DNA fragmentation [17,18]. In the anti-cancer capacity, the RONS can interfere with the cell cycle of cancer cells, inducing apoptosis, necrosis and inhibition of cancer cell growth [19,20].

It is known from literature that CAP can result in more cancer cell death or growth inhibition compared to normal cells [21,22]. The efficiency of CAP treatment is most probably due to the striking rise of intracellular RONS in cancer cells when compared to normal cells [23].

* Corresponding author.
E-mail address: annemie.bogaerts@uantwerpen.be (A. Bogaerts).

https://doi.org/10.1016/j.compbiomed.2021.104768
Received 15 July 2021; Accepted 11 August 2021
Available online 17 August 2021

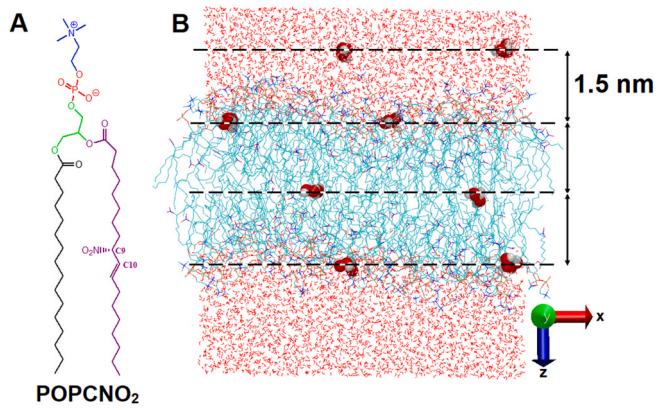

Fig. 1. (**A**) Structure of a single nitrated POPC lipid ($POPCNO_2$) used in our simulations. The atoms in blue, red, and green represent choline, phosphate, and glycerol groups, respectively. The palmitoyl (*sn*-1) and oleoyl (*sn*-2) chains are represented by black and purple colors, respectively. (**B**) Representation of one of the model membranes in our simulations. In this example, 16 H_2O_2 molecules are inserted at 4 positions of the *xy* plane separated by 1.5 nm distance in the *z*-axis (i.e., each *xy* plane contains 4 H_2O_2 molecules). Should be noted that only half of the 16 H_2O_2 molecules are visible in this membrane side view. Water molecules are represented in red (at the top and bottom of the PLB), the PLB is in the middle, and the H_2O_2 molecules are shown as van der Waals spheres (bigger beads).

The latter might occur due to some intrinsic factors, e.g., aberrant metabolism for some cancer types, mitochondrial dysfunction [24], loss of functional cytoplasmatic protein p53 that prevents cancer formation [25], and a lower cholesterol concentration inside the cell membrane. The latter increases the fluidity of the cell membrane, making it more vulnerable to nitro-oxidative stress [26–28], i.e., the overproduction of RONS inside cancer cells.

In recent years, many efforts have been devoted to understand how RONS affect cancer cells during nitro-oxidative stress. In a nitro-oxidative stress environment, RONS can directly attack the double bonds of phospholipids, the major components of the cell membrane, resulting in lipid nitro-oxidation. The lipid nitro-oxidation yields lipid products bearing functional groups, such as nitro (–NO_2), peroxynitro (–ONOO), hydroperoxide (–HOO), hydroxyl (–HO), as well as truncated acyl chains, such as aldehyde (–CHO) and carboxylic groups (–COOH) [29,30]. These nitro-oxidized products affect the microscopic and macroscopic properties of the membrane, inducing structural and conformational changes, which can lead, for example, to pore formation [31–33].

We have recently shown that nitrated lipids increase the permeability of phospholipid membranes to water by a factor three compared to oxidized lipids [34]. Nevertheless, no systematic modeling studies have been conducted to investigate the effect of nitrated lipids on the biomembrane permeability to other species, namely RONS. Computer simulations at the atomistic level have been proven as valuable complementary tools to experiments in studies of RONS-membrane interactions. Thus, in this research, we investigate the permeability of model membranes composed of nitrated lipids, using *molecular dynamics* (MD) simulations. Specifically, we study the permeation of hydrophilic (H_2O_2, HO_2, HO, ONOOH) and hydrophobic (O_2, NO_2, NO) RONS across a nitrated phospholipid bilayer (PLB) and compare the results to those available for native [35,36] and oxidized PLBs [33]. This study will hopefully contribute to a better understanding of the properties of nitrated membranes caused by different types of RONS during CAP treatment or other cancer therapies based on nitro-oxidative stress.

2. Simulation methods

2.1. Preparation of model membranes

MD simulations were performed using the software GROMACS, version 5.1.2 [37]. The united-atom GROMOS 53A6 force field was employed to describe the interatomic interactions [38]. To integrate Newton's equations of motion, a leap-frog algorithm was used with a time step of 2 fs. Periodic boundary conditions were considered in all Cartesian directions [39]. We adopted interatomic interaction parameters for nitrated lipids from our previous work [34]. Moreover, we used well-validated parameters for the description of all aforementioned RONS (i.e., H_2O_2, HO_2, HO, ONOOH, O_2, NO_2, NO) [35,40]. As a model membrane, we considered a PLB consisting of nitrated POPC (1-palmitoyl-2-oleoyl-*sn*-glycero-3-phosphocholine) lipids with the –NO_2 group at C9 position, with *S* stereocenter (i.e., $POPCNO_2$, see Fig. 1A). The PLB included 128 $POPCNO_2$ molecules, equally distributed in both layers, together with 6000 water molecules surrounding them (see Fig. 1B). In this way we obtained a fully (100%) nitrated PLB system. We did not perform simulations here for the native or oxidized PLB, but in the Results and Discussion section, we will compare with our previously obtained results for both systems [33,35,36], to evaluate the difference between nitrated, oxidized and native PLB systems.

The PLB system was equilibrated for 300 ns in the NPT ensemble (i.

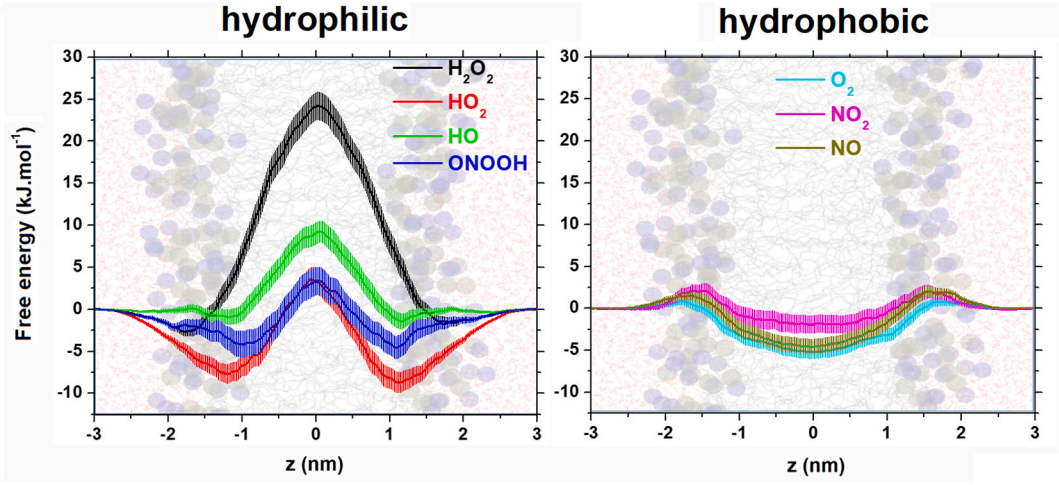

Fig. 2. FEPs of the hydrophilic and hydrophobic RONS across the nitrated ($POPCNO_2$) PLB, averaged over 150 simulations for each model membrane. The uncertainties in the profiles are represented as vertical shadow lines. For clarity, the PLB is illustrated in the background, with the headgroup region as van der Waals spheres.

Table 1
Free energy barriers (ΔG) of the various RONS across the nitrated ($POPCNO_2$) PLB, compared to those of the native, 50% peroxidized, and 50% oxidized to aldehyde PLBs, from our previous simulations (although not always for the same model membrane). For the hydrophilic RONS, the ΔG values were calculated as the difference between the free energy maximum and the free energy minimum, while for the hydrophobic RONS, as the free energy maximum at the headgroup region.

	ΔG for hydrophilic RONS (kJ.mol^{-1})			
	Nitrated POPC	Native POPC[1]	50 % peroxidized DOPC[2]	50 % aldehyde DOPC[2]
H_2O_2	26.9 ± 1.2	33 ± 4	36.4 ± 3.4	23.8 ± 1.7
HO_2	11.1 ± 1.3	19 ± 4	17.6 ± 2.6	15.8 ± 1.7
HO	10.1 ± 1.1	17 ± 4	18.6 ± 2.5	11.1 ± 1.2
ONOOH	7.5 ± 1.2	–	–	–
	ΔG for hydrophobic RONS (kJ.mol^{-1})			
	Nitrated POPC	Native DOPC[3]	50 % peroxidized DOPC[2]	50 % aldehyde DOPC[2]
NO_2	2.1 ± 0.8	1.2	–	–
NO	1.5 ± 0.5	1.0	–	–
O_2	0.9 ± 0.5	1.1	0.7	0.5

[1]ref. [35], [2]ref. [33], [3]ref. [36]

(2)

e., constant number of atoms, pressure and temperature), at 310 K and 1 bar. The temperature of the system was controlled by the Nose-Hoover thermostat [41,42], combined with a coupling constant of 0.5 ps, and the pressure was controlled by the semi-isotropic Parrinello–Rahman barostat [43], combined with a coupling constant of 2 ps and compressibility of 4.5×10^{-5} bar^{-1}. The cut-off distance for the van der Waals and Coulomb interactions was set at 1.1 nm, and the particle mesh Ewald method was applied to calculate the electrostatic interactions. This system was used in our simulations for calculation of the *free energy profiles* (FEPs) of RONS across the nitrated PLBs (see next section).

2.2. Permeation free energy profiles (FEPs)

The FEPs of RONS translocating across the $POPCNO_2$ PLBs were calculated using the *umbrella sampling* (US) method [44]. Starting structures for US (i.e., umbrella windows) were picked randomly from the last 100 ns of the 300 ns equilibration simulation. The simulated model membranes had lateral dimensions of ca. 6.7 nm parallel to the membrane surface (*xy*-plane) and ca. 7.7 nm along the bilayer normal (*z*-axis). Each model membrane was simulated five times, and in each simulation we had 30 umbrella windows separated by 0.05 nm along the *z*-axis. 16 RONS were inserted in each umbrella window, separated by 1.5 nm along the *z*-axis (see Fig. 1B, where only half of the 16 RONS are visible in the membrane side view), by gradually switching on their interactions with the rest of the system during 100 ps. The movement of the RONS was restricted along the *z*-axis by a harmonic bias with a force constant of 2000 kJ mol^{-1} nm^{-2}, and along the *xy*-plane by applying the flat-bottomed position restraint, with a radius of 0.5 nm and a force constant of 4000 kJ mol^{-1} nm^{-2}.

The US simulations were run for 6 ns using the same parameters as in the equilibration simulations (i.e., NPT ensemble, 310 K and 1 bar, see previous section). After an equilibration period of 2 ns, the collection of the free energy values took place for 4 ns. It should be noted that this time was sufficient to obtain reliable FEPs: we also performed long simulations with 15 ns of equilibration and 15 ns of analysis, and the results were similar (see e.g., the FEPs for H_2O_2 and HO in the *Supplementary data* (S) (Fig. S1)). The FEPs were built by the *weighted histogram analysis method* (WHAM) using the *gmx wham* tool [45]. The final results were obtained by averaging over five independent US simulations, i.e., five FEPs were averaged to obtain the final FEP for each RONS. In the

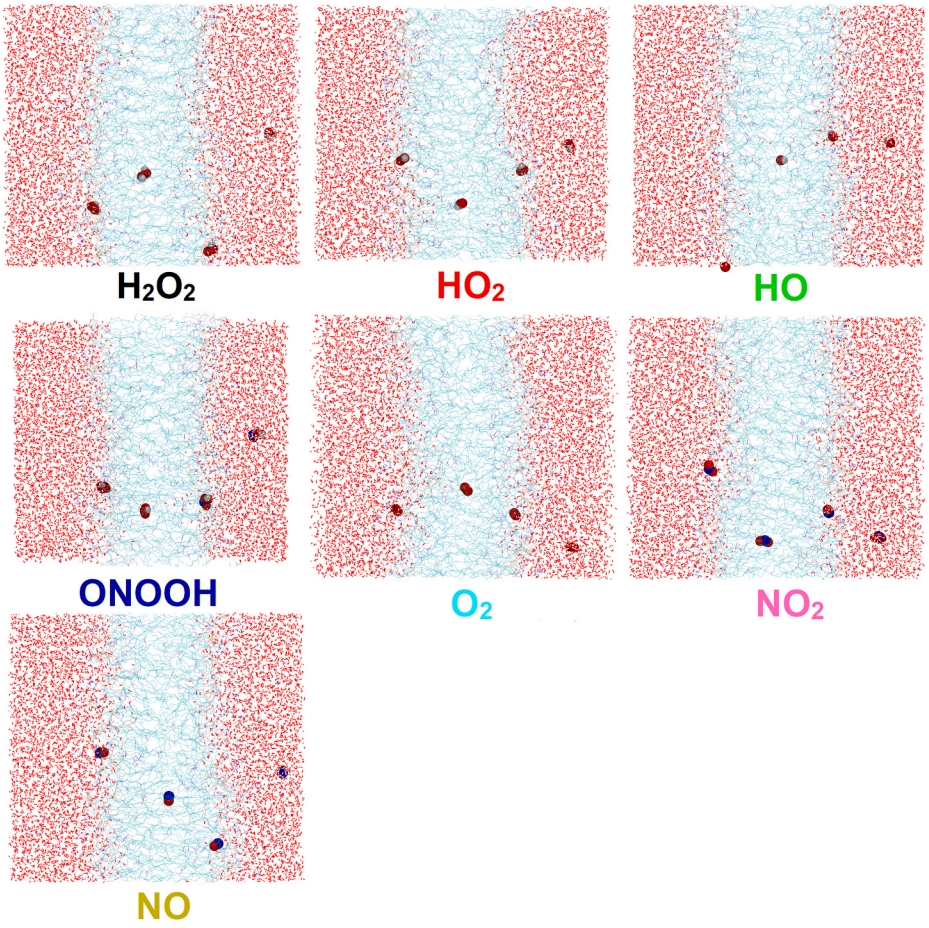

Fig. 3. Snapshots of the US simulations, showing selected RONS (van der Waals spheres) along their permeation path across the nitrated ($POPCNO_2$) PLB, and indicating that no pore formation (disruption in the structure) occurs. Color code: white, H; blue, N; and red, O. Water molecules are represented in red and the lipids in cyan.

total we performed 150 simulations for each model membrane: 30 umbrella windows x 5 replicates. The error bars (due to statistical variations) were calculated by the bootstrap method [45] (see Fig. S2).

2.3. Simulations of the RONS behavior at the water/lipid interface

Finally, we also studied the behavior of RONS at the water/lipid interface. For this purpose, 30 molecules of each of them (i.e., H_2O_2, HO_2, HO, ONOOH, O_2, NO_2, NO) were initially placed together in the aqueous phase (15 molecules in the upper aqueous phase and 15 in the bottom aqueous phase) surrounding a pre-equilibrated $POPCNO_2$ PLB. This corresponded to an initial molar fraction of ca. 0.5% for each RONS in the aqueous phase. This value is several orders of magnitude higher than experimentally measured RONS concentrations in mitochondria [46]. However, it is done to provide reasonable statistics, and it will not affect our results [47]. A 50 ns equilibration simulation was carried out for each RONS and the last 30 ns time was used for data acquisition. The same parameters were used in these equilibration runs as mentioned above.

Density profiles of RONS were built along the *z*-axis to determine their distribution at the water/lipid interface, using the *gmx density* tool of GROMACS. The trajectory of the RONS and the number of hydrogen bonds formed between the RONS and the atoms of the PLB were calculated using the *gmx traj* and *gmx hbond* tools, respectively. The area per lipid (A_L) was calculated as:

$$A_L = \frac{L_x \times L_y}{n_L} \quad (1)$$

where L_x and L_y are the box length along the *x* and *y*-axes, respectively, and n_L is the number of lipids in each leaflet (i.e., 64).

3. Results and discussion

3.1. FEPs of RONS across nitrated PLBs

Fig. 2 shows the full FEPs of various hydrophilic (H_2O_2, HO_2, HO, ONOOH) and hydrophobic (O_2, NO_2, NO) RONS across $POPCNO_2$ PLBs. Their corresponding free energy barriers (ΔG) are reported in Table 1: for the hydrophilic species, each energy barrier was calculated as the difference between the free energy maximum and the free energy minimum, while for the hydrophobic species, as the free energy maximum at the headgroup region. The higher the ΔG, the more difficult it is for RONS to translocate across the membrane. We also compare the ΔG values with the results for the native and oxidized PLB (to both peroxide and aldehyde system), obtained from our previous simulations [33,35,36]. Note that we could not always compare for the same model membrane (POPC), as our earlier simulation results were sometimes obtained for DOPC. However, the difference between POPC and DOPC should be negligible because they present similar structures. As is clear from Fig. 2, the obtained FEPs of RONS were well converged (see the comparison of the full and symmetrized FEPs in Fig. S3).

Overall, the hydrophobic RONS present clearly lower permeation barriers than the hydrophilic RONS, see Fig. 2 and Table 1. All hydrophobic RONS have their maximum energy close to the water/lipid interface (i.e., headgroup region), which mainly results from the

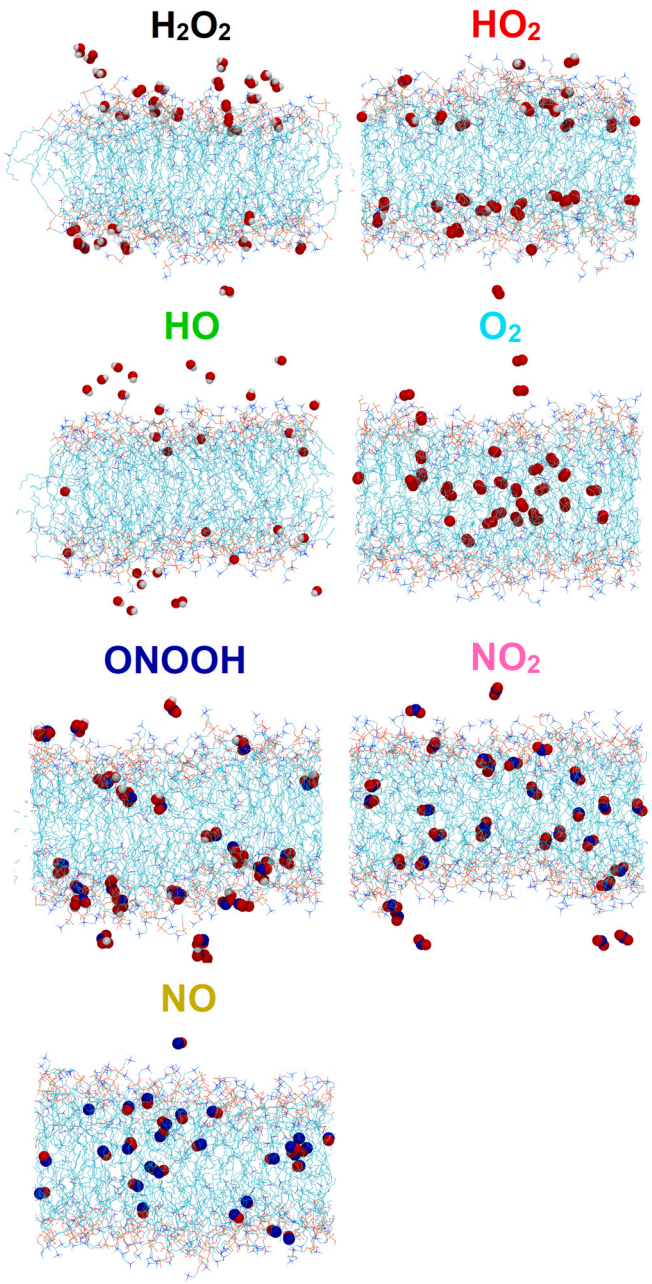

Fig. 4. Snapshots at 50 ns of the equilibrium simulations, highlighting the distributions of the various hydrophilic and hydrophobic RONS across the nitrated ($POPCNO_2$) PLB. The RONS are represented as van der Waals spheres. For the sake of clarity, the water layers on top and at the bottom are removed. For a more detailed picture of the distribution of RONS, see their trajectories obtained from the last 30 ns, shown in Fig. S5.

polarity of the headgroup region. These values are similar for all hydrophobic RONS (see Table 1 and Fig. 2). Moreover, the FEPs of the hydrophobic RONS have their minima at the PLB center (Fig. 2), reflecting the tendency of these species to accumulate in the PLB center. Experimental measurements showed that the concentration of O_2 in the membrane interior of a native PLB is approximately 3.5 times higher than in the bulk water [48]. In addition, experimental and MD simulations showed that the O_2 concentration varies as a function of the immersion depth in the membrane, with a strong dependence on temperature and on whether the membrane was in gel or fluid phase [49]. Singlet oxygen ($^1O_2$), which plays a central role in anti-cancer therapies such as photodynamic therapy [50] and plasma medicine [51], is expected to behave in a similar fashion.

For all hydrophilic RONS, the membrane acts as a permeation barrier. These results are supported by experimental evidence that H_2O_2 and HO_2 are much less permeant than O_2 [52]. In the case of H_2O_2 and HO_2, ΔG minima appear in the headgroup region due to favorable H-bond interactions with the phosphate groups and carbonyl ester groups. The minimum ΔG of ONOOH is observed even deeper in the PLB (close to the lipids) (Fig. 2), which is probably due to its specific interaction with both hydrophilic (headgroups) and hydrophobic (lipids) regions of the PLB (see below). The adsorption of HO_2 in the headgroup region is much stronger than for e.g., H_2O_2 (-7.6 ± 1.5 and -2.6 ± 1.6 kJ mol^{-1}, respectively), in agreement with previous simulations [35]. As the hydrophilic RONS penetrate into the PLB center, the free energy increases, reaching maximum values in the center of the PLB. For H_2O_2, the ΔG is by far the highest of all the hydrophilic RONS investigated (i.e., 26.9 ± 1.6 kJ mol^{-1}), but it is lower than the value for native membranes (i.e., calculated as 33 ± 4 kJ mol^{-1} [35] and 36.86 kJ mol^{-1} obtained experimentally [53]). Indeed, due to fluidity and disorder of the nitrated membrane, H_2O_2 seems to have somewhat easier access to the cell interior than for the native PLB.

Furthermore, despite the fact that ΔG is similar for both HO_2 and HO (11.1 ± 1.5 and 10.1 ± 1.3 kJ mol^{-1}, respectively), HO_2 can more easily penetrate into the headgroup region than HO: the free energy minimum in the headgroup region is -7.6 ± 1.5 and -0.9 ± 1.3 kJ mol^{-1} for HO_2 and HO, respectively. In addition, HO_2 and HO exhibit a higher ΔG than ONOOH (11.1 ± 1.5, 10.1 ± 1.3 and 7.5 ± 1.6 kJ mol^{-1}, respectively). This indicates that ONOOH may have easier access to the cell interior. Furthermore, ONOOH is a powerful oxidant, and at physiological pH (pK_a 6.5–6.8, depending on the ionic strength) it undergoes homolysis of the O–O bond, generating the radical species NO_2 and HO [54]:

As seen in Fig. 2 and Table 1, ONOOH can penetrate more easily than HO but less than NO_2. The fact that it contains a hydrophobic (NO_2) and hydrophilic (HO) part probably explains its specific interaction with the PLB, as the OH group of ONOOH tends to interact with the headgroup region, whereas the NO_2 group interacts with the lipid region, causing ONOOH to accumulate deeper into the PLB (close to the lipids) than the other hydrophilic RONS (Fig. 2).

It should be noted that the PLB structure was not disrupted during the permeation of both hydrophilic and hydrophobic RONS, i.e., the RONS permeation across the nitrated ($POPCNO_2$) PLB was not accompanied by the formation of transmembrane pores (Fig. 3), likewise native and oxidized PLBs [33,35,36]. These features are consistent with the solubility–diffusion model [55]. According to this model, hydrophilic molecules first penetrate into the membrane, at the cost of losing hydration, and then diffuse in a nearly flat energy landscape across the membrane interior. It should be mentioned that the free energy barriers calculated using different force fields tend to be somewhat different [56]. Therefore, we must pay attention to the relative values, i.e., how lipid nitration influences the overall free energy profiles of RONS (see Fig. 2 and Table 1), instead of their absolute values.

When comparing the ΔG in the nitrated PLB with the native and 50% peroxidized PLBs, the permeability of the nitrated PLB for the hydrophobic RONS is similar, i.e., within the uncertainties. However, for the hydrophilic RONS, the nitrated PLB seems more permeable than the native and 50% peroxidized PLBs (see Table 1). This result is in agreement with our previous work, where the nitrated PLB was around six- and three-fold more permeable to water than the native and peroxidized PLBs, respectively [34]. The higher accessibility of the hydrophilic RONS to the center of the nitrated PLB, and thereby the higher permeation to the cell interior, shows the important role of nitrated lipids in nitro-oxidative stress. Thus, not only the oxidation products of the PLB generated during CAP treatment must be considered, but also the nitration products. When comparing the ΔG of the nitrated PLB with the PLB that is 50% oxidized to aldehyde, their permeability is similar, but this was expected since only 2.5% of lipid aldehydes is able to increase the permeability by two orders of magnitude [32].

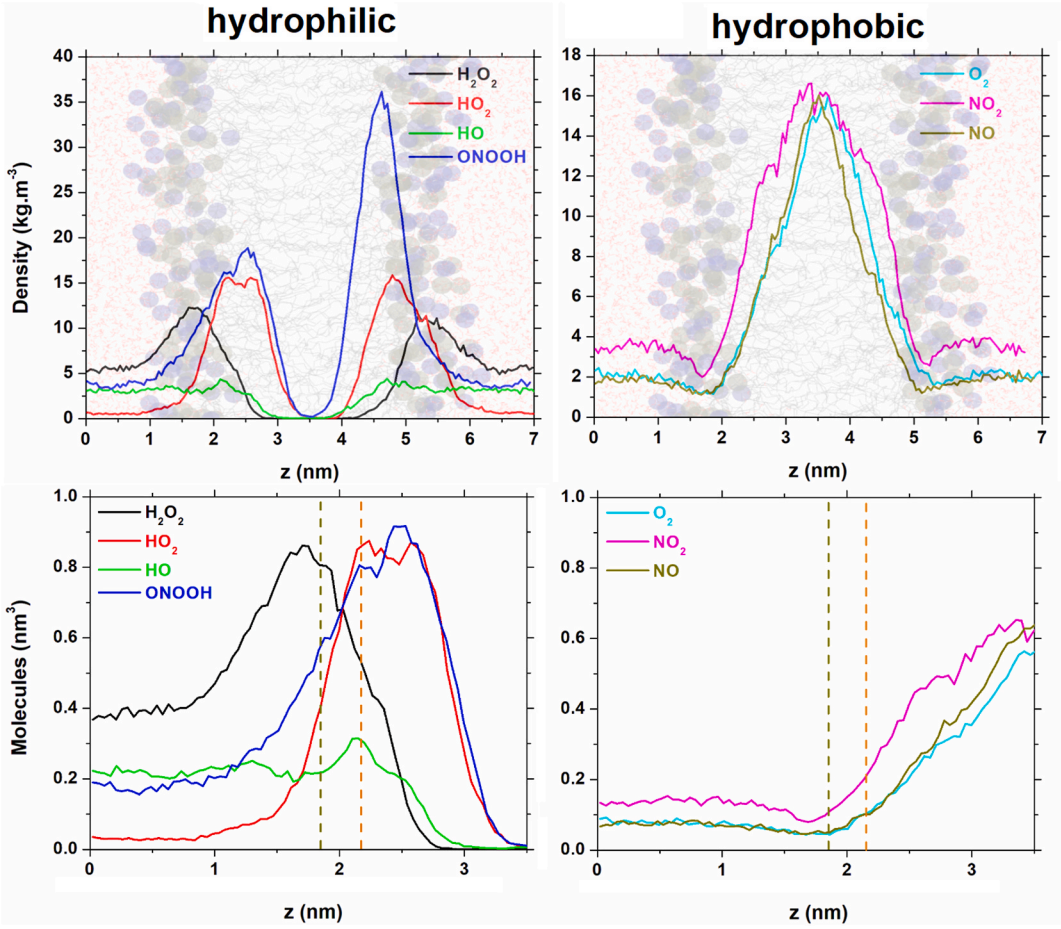

Fig. 5. Density profiles (upper panels) and number of RONS (bottom panels) of hydrophilic and hydrophobic RONS across nitrated ($POPCNO_2$) PLB. The values are calculated from the last 30 ns of the equilibrium simulations. The average positions of the phosphate groups ($z = 1.85$ nm) and carbonyl ester groups ($z = 2.17$ nm) are indicated as vertical dashed lines: dark yellow for phosphate groups and orange for carbonyl ester groups. The membrane center was set at $z = 3.5$ nm.

3.2. Distribution and dynamics of RONS over the nitrated PLB

We performed independent equilibrium simulations of RONS distributed over the nitrated PLB, in order to verify whether our US results are consistent (see Fig. S4 for a convergence check of the calculated area per lipid of the PLB with different RONS). It is important to understand the partition and dynamics of RONS at the water/lipid interface, since the reactivity is influenced not only by the RONS concentration, but also by their activity within the lipid environment, which may differ from that in the aqueous phase. In the aqueous phase and PLB, the behavior of various RONS analogues is mainly affected by hydrogen bonding, van der Waals interaction and other intermolecular interactions [35].

Fig. 4 shows the positions of the various RONS in the nitrated ($POPCNO_2$) PLB after 50 ns of simulation. We also calculated the density and number of RONS across the same system (see Fig. 5). Overall, these results corroborate our free energy profiles. HO_2 and especially ONOOH are more prone to penetrate into the PLB center than H_2O_2 and HO (see Figs. 4 and 5). Note an asymmetric profile for ONOOH, revealing that it tends to cross easily the PLB center (upper panel of Fig. 5). This is attributed to their lower free energy barriers with respect to the aqueous phase, compared to H_2O_2 and OH (cf. Fig. 2). While H_2O_2 tends to interact with the headgroup region, HO tends to remain in the aqueous phase, as demonstrated by their lower or even no free energy minima at the headgroup region (see Fig. 4 and cf. Fig. 2). The hydrophobic RONS do not interact by hydrogen bonding in the water layer and hence they can easily diffuse from the aqueous phase to the PLB center. All these results are also confirmed by the trajectories of the RONS as a function of time, presented in Fig. S5.

We also calculated the time evolution of the distances between the hydrophilic RONS and the $–NO_2$ groups of the $POPCNO_2$ lipids in the nitrated PLB (Fig. 6A). It is clear that there are more HO_2 and ONOOH species close to the $–NO_2$ groups (i.e., around 1 nm) rather than H_2O_2 and HO species (i.e., they can range between 1 and 6 nm). Interestingly, HO_2 and ONOOH establish less hydrogen bonds (H-bonds) with the oxygen atom of the $–NO_2$ groups than H_2O_2 and HO (Fig. 6B). This means that the higher permeability of HO_2 and ONOOH into the nitrated PLB is not due to the interactions between these species with the $–NO_2$ groups. Even a small number of H_2O_2 and HO species that were able to penetrate into the membrane, formed H-bonds with the $–NO_2$ groups over all the time. On the other hand, HO_2 and ONOOH penetrate directly into the membrane, without establishing many H-bonds with the $–NO_2$ groups (see Fig. 6B). The latter results are corroborated by the number of H-bonds between RONS and the water molecules: again HO_2 and ONOOH present less H-bonds than the other hydrophilic RONS (Table 2). Combining all this information with the analysis of the RONS distribution in the PLB, we can conclude that the H-bond interaction is the main mechanism of preventing translocation of RONS across the membrane, in agreement with previous simulation works [57].

4. Conclusions

We calculated the FEPs of various hydrophilic (H_2O_2, HO_2, HO, ONOOH) and hydrophobic (O_2, NO_2, NO) RONS across a nitrated PLB and compare the results to our previous simulations for native [35,36] and oxidized PLBs [33], in order to gain a better understanding about

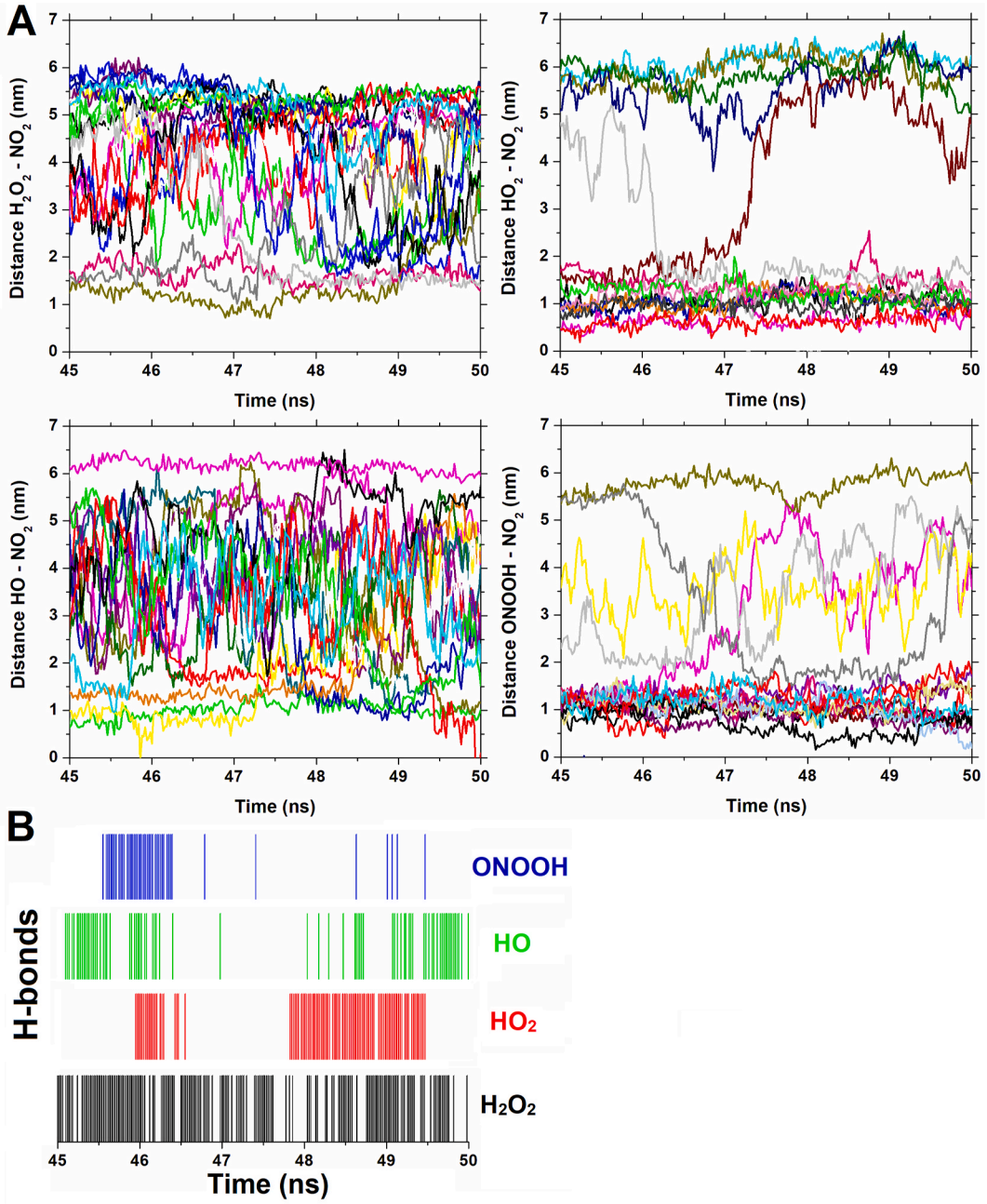

Fig. 6. (**A**) Distance between the hydrophilic RONS and the $–NO_2$ groups of the POPCNO_2 lipids in the nitrated PLB, calculated using the last 5 ns of the simulation time. Each color corresponds to an individual RONS particle. (**B**) Number of H-bonds formed between the hydrophilic RONS and the oxygen atom of the $–NO_2$ groups, also calculated using the last 5 ns of the simulation time. Colored regions indicate instants in which H-bonds existed. H-bonds were defined by donor−acceptor distances lower than 0.35 nm and angles lower than 30°.

Table 2
Average number of H-bonds between the various RONS and water molecules, calculated from the last 30 ns of simulation. H-bonds were defined by donor−acceptor distances lower than 0.35 nm and angles lower than 30°.

	Number of H-bonds	
	(as donor)	(as acceptor)
H_2O_2	20.9	32.8
HO_2	8.7	4.1 (lateral O) 5.5 (central O)
HO	20.3	18.8
ONOOH	12.3	1.1 (N) 2.8 (lateral O—N) 3.0 (central O) 7.5 (lateral O—H)
O_2	–	1.5
NO_2	–	0.3 (N) 1.4 (O)
NO	–	0.7 (N) 0.6 (O)

the permeability of nitrated membranes. We demonstrated that hydrophilic RONS like HO_2 and ONOOH are more prone to penetrate into the nitrated membrane. When compared with its homolysis products, ONOOH is more permeable than HO but less permeable than NO_2. Our FEP results were also confirmed by equilibrium simulations of RONS over nitrated membranes, and we demonstrated that H-bond interaction is the main mechanism of preventing translocation of RONS across the membrane. Overall, nitrated membranes appear to be more permeable for hydrophilic RONS than native and peroxidized membranes. This clearly indicates that nitration products of the PLB also play an important role in nitro-oxidative stress. This work may help to understand which RONS are more efficient for cancer treatment based on nitro-oxidative stress, such as photodynamic therapy and plasma medicine.

Declaration of competing interest

None Declared.

Acknowledgment

We thank University of Antwerp and Coordination of Superior Level Staff Improvement (CAPES, Brazil) for the scholarship granted and for providing the computational resources needed for completion of this work. M. Yusupov acknowledges the Flanders Research Foundation (grant 1200219N) for financial support.

Appendix A. Supplementary data

Supplementary data to this article can be found online at https://doi.org/10.1016/j.compbiomed.2021.104768.

References

[1] S.D. Bao, Q.L. Wu, R.E. McLendon, Y.L. Hao, Q. Shi, A.B. Hjelmeland, M. W. Dewhirst, D.D. Bigner, J.N. Rich, Glioma stem cells promote radioresistance by preferential activation of the DNA damage response, Nature 444 (2006) 756–760.
[2] A. Murat, E. Migliavacca, T. Gorlia, W.L. Lambiv, T. Shay, M.F. Hamou, N. de Tribolet, L. Regli, W. Wick, M.C.M. Kouwenhoven, J.A. Hainfellner, F.L. Heppner, P.Y. Dietrich, Y. Zimmer, J.G. Cairncross, R.C. Janzer, E. Domany, M. Delorenzi, R. Stupp, M.E. Hegi, Stem cell-related "self-renewal'' signature and high epidermal growth factor receptor expression associated with resistance to concomitant chemoradiotherapy in glioblastoma, J. Clin. Oncol. 26 (2008) 3015–3024.
[3] D. Barbieri, M. Boselli, F. Cavrini, V. Colombo, M. Gherardi, M.P. Landini, R. Laurita, A. Liguori, A. Stancampiano, Investigation of the antimicrobial activity at safe levels for eukaryotic cells of a low power atmospheric pressure inductively coupled plasma source, Biointerphases 10 (2015), 029519.
[4] B. Boekema, M. Stoop, M. Vlig, J. van Liempt, A. Sobota, M. Ulrich, E. Middelkoop, Antibacterial and safety tests of a flexible cold atmospheric plasma device for the stimulation of wound healing, Appl. Microbiol. Biotechnol. 105 (2021) 2057–2070.
[5] E.A. Ratovitski, X. Cheng, D. Yan, J.H. Sherman, J. Canady, B. Trink, M. Keidar, Anti-cancer therapies of 21st century: novel approach to treat human cancers using cold atmospheric plasma, Plasma Process. Polym. 11 (2014) 1128–1137.
[6] H. Yang, R. Lu, Y. Xian, L. Gan, X. Lu, X. Yang, Effects of atmospheric pressure cold plasma on human hepatocarcinoma cell and its 5-fluorouracil resistant cell line, Phys. Plasmas 22 (2015) 122006.
[7] M. Amini, J. Ghanavi, P. Farnia, M. Karimi, H. Ghomi, In vitro antiproliferative activity of cold atmospheric plasma on small-cell lung carcinoma, Biomed. Biotechnol. Res. J. 4 (2020) 76–80.
[8] A. Sadoughi, S. Irani, S. Bagheri-Khoulenjani, S.M. Atyabi, N. Olov, Cold atmospheric plasma modification of curcumin loaded in tri-phosphate chitosan nanoparticles enhanced breast cancer cells apoptosis, Polym. Adv. Technol. 32 (2020) 31–40.
[9] A. Lin, Y. Gorbanev, J. De Backer, J. Van Loenhout, W. Van Boxem, F. Lemière, P. Cos, S. Dewilde, E. Smits, A. Bogaerts, Non-thermal plasma as a unique delivery system of short-lived reactive oxygen and nitrogen species for immunogenic cell death in melanoma cells, Adv. Sci. 6 (2019) 1802062.
[10] A. Privat-Maldonado, Y. Gorbanev, S. Dewilde, E. Smits, A. Bogaerts, Reduction of human glioblastoma spheroids using cold atmospheric plasma: the combined effect of short- and long-lived reactive species, Cancers 10 (2018) 394.
[11] R. Verloy, A. Privat-Maldonado, E. Smits, A. Bogaerts, Cold atmospheric plasma treatment for pancreatic cancer - the importance of pancreatic stellate cells, Cancers 12 (2020) 2782.
[12] R. Rutkowski, M. Schuster, J. Unger, C. Seebauer, H.R. Metelmann, T. von Woedtke, K.D. Weltmann, G. Daeschlein, Hyperspectral imaging for in vivo monitoring of cold atmospheric plasma effects on microcirculation in treatment of head and neck cancer and wound healing, Clin. Plasma Med. 7–8 (2017) 52–57.
[13] X. Lu, G.V. Naidis, M. Laroussi, S. Reuter, D.B. Graves, K. Ostrikov, Reactive species in non-equilibrium atmospheric-pressure plasmas: generation, transport, and biological effects, Phys. Rep. 630 (2016) 1–84.
[14] G. Daeschlein, M. Napp, S. Lutze, A. Arnold, S. von Podewils, D. Guembel, M. Junger, Skin and wound decontamination of multidrug-resistant bacteria by cold atmospheric plasma coagulation, J. Dtsch. Dermatol. Ges. 13 (2015) 143–150.
[15] E. Turrini, R. Laurita, E. Simoncelli, A. Stancampiano, E. Catanzaro, C. Calcabrini, G. Carulli, M. Rousseau, M. Gherardi, F. Maffei, V. Cocchi, M. Lenzi, V. Pellicioni, P. Hrelia, V. Colombo, C. Fimognari, Plasma-activated medium as an innovative anticancer strategy: insight into its cellular and molecular impact on in vitro leukemia cells, Plasma Process. Polym. 17 (2020), e2000007.
[16] H. Zhang, S.D. Xu, J.S. Zhang, B. Li, D.X. Liu, L. Guo, Z.J. Liu, D.H. Xu, *Synergistic anticancer effects of different combinations of He+O_2 plasma jet and doxorubicin on A375 melanoma cells*, Plasma Process. Polym. (2021), e2000239.
[17] H. Lu, S. Patil, K.M. Keener, P.J. Cullen, P. Bourke, Bacterial inactivation by high-voltage atmospheric cold plasma: influence of process parameters and effects on cell leakage and DNA, J. Appl. Microbiol. 116 (2014) 784–794.
[18] X.Y. Liao, D.H. Liu, T. Ding, Nonthermal plasma induces the viable-but-nonculturable state in Staphylococcus aureus via metabolic suppression and the oxidative stress response, Appl. Environ. Microbiol. 86 (2020) e02216–e02219.
[19] O. Volotskova, T.S. Hawley, M.A. Stepp, M. Keidar, Targeting the cancer cell cycle by cold atmospheric plasma, Sci. Rep. 2 (2012) 636.
[20] N. Gaur, H. Kurita, J.S. Oh, S. Miyachika, M. Ito, A. Mizuno, A.J. Cowin, S. Allinson, R.D. Short, E.J. Szili, On cold atmospheric-pressure plasma jet induced DNA damage in cells, J. Phys. D Appl. Phys. 54 (2021), 035203.
[21] D. Yan, Toward understanding the selective anticancer capacity of cold atmospheric plasma—a model based on aquaporins, Biointerphases 10 (2015), 040801.
[22] E. Biscop, A. Lin, W. Van Boxem, J. Van Loenhout, J. De Backer, C. Deben, S. Dewilde, E. Smits, A. Bogaerts, Influence of cell type and culture medium on determining cancer selectivity of cold atmospheric plasma treatment, Cancers 11 (2019) 1287.
[23] S.J. Kim, H.M. Joh, T.H. Chung, Production of intracellular reactive oxygen species and change of cell viability induced by atmospheric pressure plasma in normal and cancer cells, Appl. Phys. Lett. 103 (2013) 153705.
[24] A.C. Boese, S.M. Kang, Mitochondrial metabolism-mediated redox regulation in cancer progression, Redox Biology 42 (2021) 101870.
[25] I. Hernandez-Resendiz, A. Roman-Rosales, E. Garcia-Villa, A. Lopez-Macay, E. Pineda, E. Saavedra, J.C. Gallardo-Perez, E. Alvarez-Rios, P. Gariglio, R. Moreno-Sanchez, S. Rodriguez-Enriquez, Dual regulation of energy metabolism by p53 in

human cervix and breast cancer cells, Biochim. Biophys. Acta Mol. Cell Res. 1853 (2015) 3266–3278.
[26] F. de Meyer, B. Smit, Effect of cholesterol on the structure of a phospholipid bilayer, Proc. Natl. Acad. Sci. U.S.A. 106 (2009) 3654–3658.
[27] J. Van der Paal, E.C. Neyts, C.C.W. Verlackt, A. Bogarts, Effect of lipid Peroxidation on membrane Permeability of Cancer and normal cells Subjected to oxidative stress, Chem. Sci. 7 (2016) 489–498.
[28] J. Van der Paal, C. Verheyen, E.C. Neyts, A. Bogaerts, Hampering effect of cholesterol on the permeation of reactive oxygen species through phospholipids bilayer: possible explanation for plasma cancer selectivity, Sci. Rep. 7 (2017) 39526.
[29] M.H. Brodnitz, W.W. Nawar, I.S. Fagerson, Autoxidation of saturated fatty acids.I. initial products of autoxidation of methyl, *Palmitate*. Lipids 3 (1968) 59–64.
[30] P. Jurkiewicz, A. Olzynska, L. Cwiklik, E. Conte, P. Jungwirth, F.M. Megli, M. Hof, Biophysics of lipid bilayers containing oxidatively modified phospholipids: insights from fluorescence and EPR experiments and from MD simulations, Biochim. Biophys. Acta 1818 (2012) 2388–2402.
[31] P. Boonnoy, V. Jarerattanachat, M. Karttunen, J. Wong-ekkabut, Bilayer deformation, pores, and micellation induced by oxidized lipids, J. Phys. Chem. Lett. 6 (2015) 4884–4888.
[32] K.A. Runas, N. Malmstadt, Low levels of lipid oxidation radically increase the passive permeability of lipid bilayers, Soft Matter 11 (2015) 499–505.
[33] M. Yusupov, J. Van der Paal, E.C. Neyts, A. Bogaerts, Synergistic effect of electric field and lipid oxidation on the permeability of cell membranes, Biochim. Biophys. Acta Gen. Subj. 1861 (2017) 839–847.
[34] M.C. Oliveira, M. Yusupov, A. Bogaerts, R.M. Cordeiro, How do nitrated lipids affect the properties of phospholipid membranes? Arch. Biochem. Biophys. 695 (2020) 108548.
[35] R.M. Cordeiro, Reactive oxygen species at phospholipid bilayers: distribution, mobility and permeation, Biochim. Biophys. Acta 1838 (2014) 438–444.
[36] J. Razzokov, M. Yusupov, R.M. Cordeiro, A. Bogaerts, Atomic scale understanding of the permeation of plasma species across native and oxidized membranes, J. Phys. D Appl. Phys. 51 (2018) 365203.
[37] D. Van Der Spoel, E. Lindahl, B. Hess, G. Groenhof, A.E. Mark, H.J.C. Berendsen, GROMACS: fast, flexible, and free, J. Comput. Chem. 26 (2005) 1701–1718.
[38] C. Oostenbrink, A. Villa, A.E. Mark, W.F. Van Gunsteren, A biomolecular force field based on the free enthalpy of hydration and solvation: the GROMOS force-field parameter sets 53A5 and 53A6, J. Comput. Chem. 25 (2004) 1656–1676.
[39] D.N. Theodorou, U.W. Suter, Geometrical considerations in model systems with periodic boundaries, J. Chem. Phys. 82 (1985) 955–966.
[40] R.M. Cordeiro, Reactive oxygen and nitrogen species at phospholipid bilayers: peroxynitrous acid and its homolysis products, J. Phys. Chem. B 122 (2018) 8211–8219.
[41] S. Nose, A molecular-dynamics method for simulations in the canonical ensemble, Mol. Phys. 52 (1984) 255–268.
[42] W.G. Hoover, Canonical dynamics - equilibrium phase-spacedistributions, Phys. Rev. A: At., Mol., Opt. Phys. 31 (1985) 1695–1697.
[43] M. Parrinello, A. Rahman, Polymorphic Transitions in Single-Crystals - a new molecular-dynamics method, J. Appl. Phys. 52 (1981) 7182–7190.
[44] J. Kästner, *Umbrella sampling*, WIREs comput, Mol. Sci. 1 (2011) 932–942.
[45] J.S. Hub, B.L. de Groot, D. van der Spoel, g_wham — a free weighted histogram analysis implementation including robust error and autocorrelation estimates, J. Chem. Theor. Comput. 6 (2010) 3713–3720.
[46] E. Cadenas, K.J. Davies, Mitochondrial free radical generation, oxidative stress, and aging, Free Radic. Biol. Med. 29 (2000) 222–230.
[47] F. Fogolari, A. Corazza, S. Toppo, S.C.E. Tosatto, P. Viglino, F. Ursini, G. Esposito, Studying interactions by molecular dynamics simulations at high concentration, J. Biomed. Biotechnol. 2012 (2012) 303190.
[48] W.K. Subczynski, J.S. Hyde, Concentration of oxygen in lipid bilayers using a spin-label method, Biophys. J. 41 (1983) 283–286.
[49] I.O.L. Bacellar, R.M. Cordeiro, P. Mahlingb, M.S. Baptista, B. Röderb, S. Hackbarth, Oxygen distribution in the fluid/gel phases of lipid membranes, Biochim. Biophys. Acta Biomembr. 1861 (2019) 879–886.
[50] L. Huang, S.J. Zhao, J.S. Wu, L. Yu, N. Singh, K. Yang, M.H. Lan, P.F. Wang, J. S. Kim, Photodynamic therapy for hypoxic tumors: advances and perspectives, Coord. Chem. Rev. 438 (2021) 213888.
[51] M. Keidar, Plasma Cancer Therapy, first ed., Springer Nature, Switzerland, 2020.
[52] M.N. Moller, E. Cuevasanta, F. Orrico, A.C. Lopez, L. Thomson, A. Denicola, Diffusion and transport of reactive species across cell membranes, Bioact. Lipids Health Disease 1127 (2019) 3–19.
[53] J.C. Mathai, V. Sitaramam, Stretch sensitivity of transmembrane mobility of hydrogen peroxide through voids in the bilayer-Role of cardiolipin, J. Biol. Chem. 269 (1994) 17784–17793.
[54] W.H. Koppenol, P.L. Bounds, T. Nauser, R. Kissner, H. Rüegger, Peroxynitrous acid: controversy and consensus surrounding an enigmatic oxidant, Dalton Trans. 41 (2012) 13779–13787.
[55] S.J. Marrink, H.J.C. Berendsen, Simulation of water transport through a lipid membrane, J. Phys. Chem. 98 (1994) 4155–4168.
[56] A.N. Leonard, E. Wang, V. Monje-Galvan, J.B. Klauda, Developing and testing of lipid force fields with applications to modeling cellular membranes, Chem. Rev. 119 (2019) 6227–6269.
[57] Y. Hu, T. Zhao, L. Zou, X. Wang, Y. Zhang, Molecular dynamics simulations of membrane properties affected by plasma ROS based on the GROMOS force field, Biophys. Chem. 253 (2019) 106214.